

Extraction and Visualization of Poincaré Map Topology for Spacecraft Trajectory Planning

Category: Research

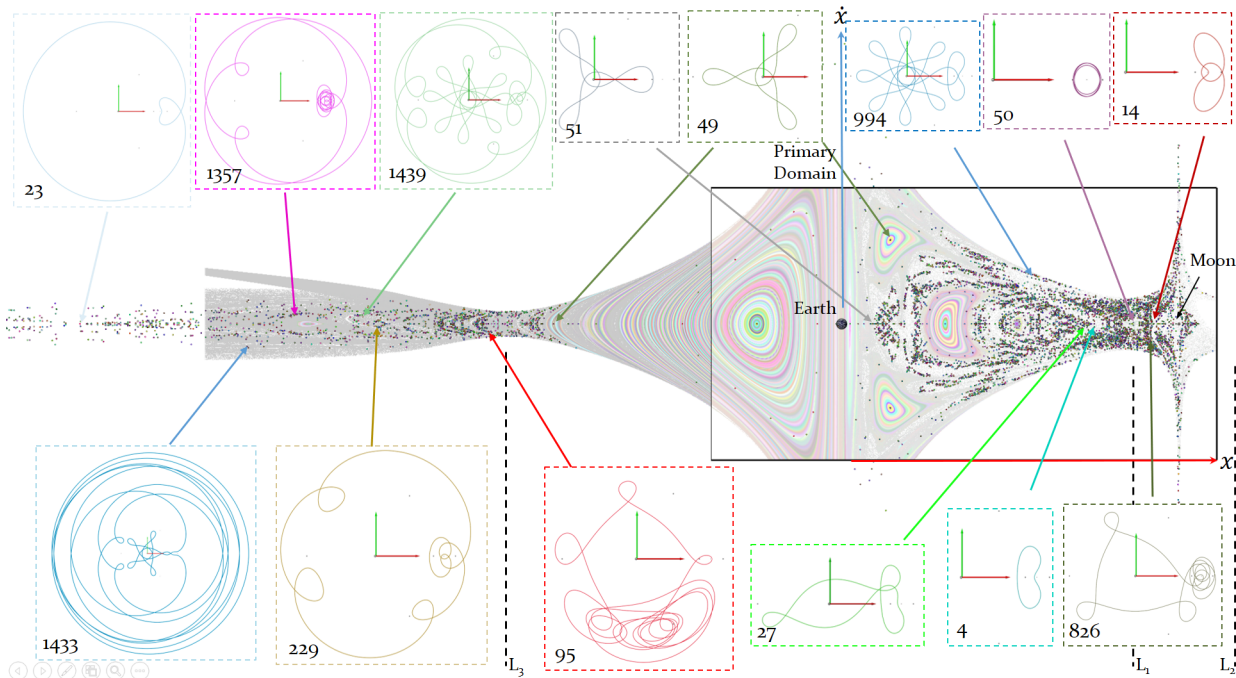


Fig. 1. Fixed points in the Earth-Moon system at $C = 2.96$. This is the collective result for the trials in Table 2.

Abstract—Astrodynamics, the application of celestial mechanics to predict motion of space vehicles, incorporates many dynamical models where analysis and design is assisted with Poincaré maps. Planning a low-cost spacecraft trajectory that satisfies mission constraints often involves selecting a suitable path through the interconnected web of Poincaré map structures such as fixed points (or periodic orbits) and invariant manifolds present in multi-body gravitational systems. Unfortunately, existing methods fail to extract this topological skeleton due to violated setup assumptions and strong numerical sensitivities. This paper presents several important algorithmic contributions that address the limitations of existing techniques and enables, for the first time, autonomous and tractable Poincaré map topology extraction in astrodynamics problems. A practical application of the topological skeleton for spacecraft trajectory planning in the circular restricted three-body problem (CRTBP) is then presented, in which the visualization of invariant manifolds is shown to enable selection of nearly no-cost transitions between periodic orbits, thereby opening new design options during path planning.

Index Terms—Astrodynamics, trajectory planning and design, Poincaré map, dynamical systems, topology extraction, invariant manifolds, chaos.

1 INTRODUCTION

Space missions collect scientific data about celestial bodies and astronomical phenomena, yielding new knowledge and insight about the origins of the universe. The design of a spacecraft trajectory is the key to success of any mission. The spacecraft path must deliver the scientific objectives under the constraints imposed by the laws of physics and a targeted mission price. Although many factors influence the mission cost, the price is strongly driven by the spacecraft mass [20], which is represented by three fundamental components – payload, support structure, and propellant. The payload is the collection of science instruments required to deliver the mission data whereas the support structure consists of the spacecraft operational equipment (e.g., bus, antenna, engines, propellant tanks, solar arrays, etc). Course corrections or maneuvers are accomplished by performing a change in spacecraft velocity (or ΔV) while expelling propellant. Although propellant is necessary to perform maneuvers, less propellant mass is typically

preferred in favor of more payload mass. Such a trade-off produces more scientific return for the mission while potentially reducing the overall monetary cost. In this context, the role of a spacecraft trajectory designer is to devise a pathway that minimizes the amount of propellant required to transport the vehicle to mission objectives.

Leveraging chaotic dynamics available in multi-body gravitational models permits small maneuvers to impart large alterations in downstream spacecraft destinations. Thus, spacecraft trajectory designers often resort to naturally existing dynamics in such nonlinear multi-body models as ideal transfer options to minimize propellant usage. Unfortunately, pinpointing favorable maneuver locations in position-space visualizations is quite difficult since orbital structures repeatedly overlap and information about velocity magnitudes is limited due to the high-dimensional nature of the problem. As an alternative, pertinent dynamical flow is observed from a global perspective via a sur-

face of section utilizing the Poincaré map (or first-return mapping). The resulting Poincaré section preserves a phase-space snapshot of all behavior that crosses a given hyperplane defining the surface of section. The problem dimensionality is then reduced into a tractable arena (2D or 3D) while also highlighting velocity differentials. Existing Poincaré map topology extraction methods [17, 13] exploit local linear models to extract topological structures embedded in nonlinear dynamics. Knowing the topological skeleton that reflects how orbital structures connect freely or with small ΔV s supplies spacecraft path-planning with a plethora of novel options and pathways that save on propellant usage (typically at the expense of extended flight time).

Yet, the automatic extraction of Poincaré map topology within multi-body gravitational models remains challenging due to numerical sensitivities during path simulation and violated assumptions in the Poincaré map. This paper presents important contributions to Poincaré map topology extraction that address the specific numerical and structural challenges raised by multi-body gravitational systems. Adaptive computation techniques are applied for enhanced characterization of behavior and the detection of periodic orbits. A similar adaptive strategy is employed for the development of invariant manifolds, resulting in a tree-like data structure that simplifies invariant manifold interaction during a design process.

Precise knowledge of the Poincaré map topology provides a detailed structure for planning spacecraft trajectories. Natural transfers between periodic orbits residing within chaotic flow spaces exist and are often exploited for transfer designs with minimal maneuver costs [12, 10, 18, 7]. Most of the structure available from previous work, however, relies heavily on the known periodic orbits of multi-body dynamics. The fixed point extraction solution described in this paper uncovers a wealth of previously unknown periodic orbits that open transfer design possibilities. In addition, our invariant manifold generation technique allows us to interactively identify robust and accurate navigation pathways across chaotic regions, which in turn, enables the rapid definition of free-flowing connections between any two arbitrary unstable orbits. Over all, the proposed visual computing framework greatly expands the design space for mission development and can lead to design previously unknown to astrodynamics.

2 CIRCULAR RESTRICTED THREE-BODY PROBLEM

The gravitational model considered in this paper pertains to the motion of a spacecraft (or other exceptionally small body) under the influence of two celestial bodies that form an orbital system (e.g., Earth and Moon, Sun and Earth, or Saturn and Titan). The motion of a spacecraft under the influence of the combined gravitational field is then simplified to the area-preserving circular restricted three-body problem (CR3BP) model. Assume a pair of gravitating bodies (P_1 and P_2 with corresponding masses $m_1 > m_2$) move about the common barycenter in circular orbits; spacecraft flight is then simulated with the CR3BP equations of motion such that the path evolves only in 2D. Let the gravity parameter, μ , represent a ratio of masses or $\mu = m_2/(m_1 + m_2)$. The state vector $\mathbf{x} = [x, y, \dot{x}, \dot{y}]^T$ (with $\dot{\cdot}$ denoting the time derivative $\frac{d\cdot}{dt}$) relates the position and velocity of a small body ($m \ll m_1, m_2$) with respect to the barycenter. Coordinates are expressed in a rotating reference frame with the origin at the barycenter where the axes $\hat{\mathbf{x}}$ aligns with the $\overrightarrow{P_1 P_2}$ line and $\hat{\mathbf{y}}$ points concurrent to the velocity vector of P_2 with respect to P_1 . Define the distances from the spacecraft to P_1 and P_2 as

$$r_1 = ((x + \mu)^2 + y^2)^{\frac{1}{2}} \text{ and } r_2 = ((x - 1 + \mu)^2 + y^2)^{\frac{1}{2}}, \quad (1)$$

respectively. Note that position (x, y) and velocity (\dot{x}, \dot{y}) coordinates are expressed in nondimensional units such that the quantities possess similar magnitudes [2]. For reference, a nondimensional position unit in the Earth-Moon (EM) system is equivalent to 384388.174 km whereas a nondimensional velocity unit is 1.02456261 km/s. Then, a pseudo-potential value (Υ) is realized as a function of only position such that

$$\Upsilon(x, y) = \frac{1 - \mu}{r_1} + \frac{\mu}{r_2} + \frac{1}{2}(x^2 + y^2), \quad (2)$$

for planar motion. The CR3BP model is then evaluated as the second-order system described by

$$\ddot{x} - 2\dot{y} = \frac{\partial \Upsilon}{\partial x}, \quad (3)$$

$$\ddot{y} + 2\dot{x} = \frac{\partial \Upsilon}{\partial y}, \quad (4)$$

which defines an ODE on the state vector \mathbf{x} . Note, a third out-of-plane (or z) component of flow also exists but is decoupled from planar motion [15, 2]. The Hamiltonian in the CR3BP model is the Jacobi constant C :

$$C = 2\Upsilon(x, y) - (\dot{x}^2 + \dot{y}^2), \quad (5)$$

in the planar sense with the total planar velocity $V = (\dot{x}^2 + \dot{y}^2)^{\frac{1}{2}}$ [15, 2]. The constancy of C implies that the system is time-invariant and area-preserving [9].

3 TOPOLOGICAL STRUCTURE IN POINCARÉ MAPS

We summarize in the following the basic results from dynamical systems theory that are relevant to our work. Note that we restrict our considerations to *Hamiltonian systems with two degrees of freedom* since this category encompasses the planar CR3BP. We refer the reader to classical references on the subject for further detail [6, 9].

A dynamical system associated with a vector field \mathbf{v} defines a *flow map* \mathbf{x}_f with $\dot{\mathbf{x}}_f = \mathbf{v}(\mathbf{x}_f)$ such that $\mathbf{x}_f(t, t_0, \mathbf{x}_0)$ describes the transport from an initial state \mathbf{x}_0 at t_0 to its later state at time t .

Let Σ represent a hyperplane that is transverse to the flow and let \mathbf{x}_0 be an initial state on Σ . The Poincaré map, or the first-return map, is defined as the mapping

$$P(\mathbf{x}_0) := \mathbf{x}_0 \mapsto P_\Sigma(\mathbf{x}_0), \quad (6)$$

where $P_\Sigma(\mathbf{x}_0)$ represents the first crossing of Σ by the trajectory starting at \mathbf{x}_0 . Multiple iterates of the Poincaré map are then computed by compounding the first return map, e.g., $P^p(\mathbf{x}_0) = P_\Sigma(P_\Sigma(\dots P_\Sigma(\mathbf{x}_0)))$ for p iterates. Both the initial state and first return to Σ are shown on the green hyperplane in Figure 2(a).

Three dynamic behaviors co-exist on a Poincaré map for a so-called *near-integrable system* (e.g., the planar CR3BP): *periodicity*, *quasi-periodicity*, and *chaos*. Visible in Figure 2(a), a periodic state, \mathbf{x}^* , returns to the same state through the Poincaré map, i.e.,

$$P^p(\mathbf{x}^*) = \mathbf{x}^*, \quad (7)$$

where p represents the number of returns required for a p -periodic trajectory to complete an orbit. These p distinct returns are called *fixed points* of the Poincaré map, whereby fixed points with nearby rotational behavior are called *centers* and those with hyperbolic attraction and repulsion are called *saddles*. A representative schematic topological skeleton of a Poincaré map with saddle-type and center-type behaviors is displayed in Figure 2(b). Quasi-periodic structures are characterized as closed curves on the Poincaré section that encircle the centers. Bounding trajectories, known as KAM curve, mark the transition from quasi-periodic behavior to chaotic behavior. Stable and unstable manifolds emerge from the saddle points indicating dynamical flow into and out of the periodic orbits, respectively. A pivotal element of map topology, especially for low maneuver-cost trajectory design problems, is the connection between saddle points via the unstable-to-stable manifold transition. In fact, stable and unstable manifolds generally intersect an infinite number of times, creating the chaotic tangles as seen in Figure 2(b).

For integrable and near-integrable Hamiltonian systems with two-degrees of freedom, considering the flow along a standard torus provides an abstract interpretation of the dynamical behavior. The motion along the torus is then characterized by the so-called *winding number* $w = \frac{\omega_1}{\omega_2}$, where ω_1 and ω_2 are the poloidal and toroidal rotation frequencies, respectively. The winding number permits to classify trajectories: numbers with exact integer ratios $w = \frac{q}{p}$, $p, q \in \mathbb{N}^*$ correspond to periodic orbits. In this case q corresponds to the number of poloidal

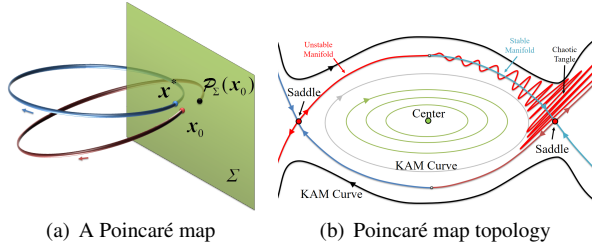


Fig. 2. Available topological structure associated with a Poincaré map in a near-integrable dynamical system [17, 6, 9].

rotations performed during p toroidal rotations and if p and q are mutually prime, p is the period associated with the fixed point. In contrast, quasi-periodic trajectories possess irrational winding number: a quasi-periodic orbit will never trace exactly the same path along the torus but will visit a dense portion of the torus as the trajectory evolves. Finally, in the case of chaotic trajectories, the winding number is undefined.

Since analytical equations of motion exist for the CR3BP (Equations 3), the state transition matrix (STM) evaluated from an initial time t_0 to a later time t is defined as

$$\Phi(t, t_0) = \frac{\partial \mathbf{x}_f}{\partial \mathbf{x}_0}. \quad (8)$$

Practically the first-order approximation of the STM is propagated simultaneously with the planar CR3BP model (Equations 3 and 4) via the matrix expression

$$\frac{\partial \Phi(t, t_0)}{\partial t} = \dot{\Phi}(t, t_0) = A(t)\Phi(t, t_0), \quad (9)$$

where $A(t)$ is the spatial gradient of \mathbf{v} . In the vicinity of periodic orbits, the full-period STM matrix $\mathcal{M} = \Phi(T, 0)$, called the *monodromy* matrix, offers a linearized description of the local dynamics and provides the information needed to determine the invariant subspaces associated with stable and unstable manifolds. The equation relating a linear variation from a fixed point through a full period, T , is described by

$$\partial \mathbf{x}_f = \mathcal{M} \partial \mathbf{x}_0 = \Phi(T, 0) \partial \mathbf{x}_0, \quad (10)$$

The stability characteristics of a fixed point are determined by the eigenvalues of the matrix \mathcal{M} . The local eigenspaces of the fixed point (E^i with $i = S, C, U$ for stable, center, and unstable, respectively) create the linear approximation of the global manifolds W^i at the fixed point location. Because the determinant of the monodromy matrix in an area preserving map is one, its eigenvalues must exist as reciprocal pairs. The eigenvalues determine the eigenspace type via

$$E^S \in \|\lambda_i\| < 1, E^C \in \|\lambda_i\| = 1, E^U \in \|\lambda_i\| > 1. \quad (11)$$

An alternative stability classification is possible through a stability index, v_{SI} , defined as

$$v_{SI} = \frac{1}{2}(\lambda + \lambda^{-1}), \quad (12)$$

where λ is an eigenvalue of \mathcal{M} . Orbits are unstable when $|v_{SI}| > 1.0$ and stable otherwise. In practice, the planar stability index is preferably computed with

$$v_{SI} = \frac{1}{2}(\text{tr}(\mathcal{M}) - 2), \quad (13)$$

which is both simpler and more numerically reliable than eigenanalysis.

4 PRIOR WORK ON POINCARÉ MAP TOPOLOGY

Our proposed solution for the visual analysis of the CR3BP topology leverages prior work on Poincaré map topology visualization [17] and its recent extension to multi-body gravitational environments [13]. We summarize here the main steps of their method.

Poincaré map sampling. The first step consists in a regular sampling of the Poincaré map. The corresponding numerical integration is carried out for a fairly large number of toroidal revolutions and all the intermediate returns to the Poincaré section are recorded for the next phase.

Trajectory classification. The next step calculates the winding number associated with each computed trajectory. Here, the large number of iterations of the Poincaré map performed previously allows for the winding number approximation, which is updated after each step of the integration, to converge. A best rational approximation of this number $w = \frac{q}{p}$ is then determined such that the denominator $p \in \mathbb{N}$ does not exceed a user-defined maximum period p_{max} for the analysis.

In the specific context of the CR3BP, Schlei *et al.* [13] proposed to jointly consider three distinct winding numbers computed directly in the standard rotating coordinates of the problem. Indeed they showed that the combination of these three numbers offers a refined assessment of the dynamics. Specifically, a triplet $\mathbf{W} = (w_{x\dot{x}}, w_{xy}, w_{\dot{y}})$ is computed for each trajectory where the individual ratios are

$$w_{x\dot{x}} = \frac{2\pi n}{\theta_{x\dot{x}}}, \quad w_{xy} = \frac{2\pi n}{\theta_{xy}}, \quad w_{\dot{y}} = \frac{2\pi n}{\theta_{\dot{y}}} \quad (14)$$

and the angles θ_i measure the accumulated poloidal rotation around the system's barycenter in the corresponding dimensions during n toroidal rotations.

Cellwise index computation. The primary purpose of the winding number computation in the previous step is to narrow down the range of periods that need to be considered in the analysis of the individual sampling cells. Specifically, in each cell the Poincaré index corresponding to the vector-valued (displacement) mapping

$$\Delta = \mathcal{P}^p(\mathbf{x}) - \mathbf{x}. \quad (15)$$

is computed via adaptive sampling of the Poincaré map along the edges of the cell for each of the periods associated with the four vertices in the previous step. If the sampling resolution was chosen fine enough in the first step, the resulting index values are expected to be either -1 , 0 , or $+1$, whereby -1 indicates the presence of a saddle-type fixed point, $+1$ indicates a center-type fixed point, and 0 suggests that no fixed point is present in the cell.

Fixed point extraction. If a non-zero index has been computed, a fixed point search is performed in the cell at the corresponding period. A fixed point corresponds to a zero value of the displacement map Δ and a Newton iterative method is used to determine the corresponding location. A key requirement to achieve convergence of the Newton search is the identification of a good first guess. While the initial method [17] used a simple subsampling of the cell to select a good candidate, a multiple shooting method was added to this solution to further reinforce the numerical convergence in the face of sensitive dynamics in the CR3BP [13].

Manifold extraction. Once the location of a fixed point of \mathcal{P}^p has been resolved with sufficient accuracy (as determined by an upper bound on $\|\Delta\|$), the linear type of the fixed point (center or saddle) is determined through Eigenanalysis of the monodromy matrix (*i.e.*, the spatial derivative $\nabla_{\mathbf{x}} \mathcal{P}^p$). If the Eigenvalues correspond to a saddle type (see Equation 11), the corresponding invariant manifolds are then constructed through a succession of shooting problems [4] and their progression stops when they approach another saddle-type fixed point.

5 ROBUST AND EFFICIENT TOPOLOGY EXTRACTION IN CR3BP

While prior work [13] offers a general framework for Poincaré map topology extraction, it suffers from a number of significant limitations that make it unsuitable for the visual analysis of the CR3BP that we present in Section 6. We describe in the following a number of algorithmic and numerical solutions that we devised to address these shortcomings.

5.1 Adaptive Poincaré map sampling

To permit a reliable detection of potential fixed points, the Poincaré index of the displacement map Δ (Equation 15) must be evaluated around areas of the map that are small enough to contain at most a single fixed point for the considered period [14]. Hence, a very high resolution sampling yielding tiny cells is typically desirable. However, this approach is computationally prohibitive and a more subtle data-driven sampling is needed.

We first observe that the winding number is a locally smoothly varying characteristic parameter, within regions of regular dynamics. Therefore, the variance in the winding number set \mathbf{W} (Equation 14) can be utilized to determine when to subdivide a cell. Ideally, a cell that isolates fixed points should not exhibit significant variations in its associated \mathbf{W} values. Practically we adopt an adaptive refinement strategy for the Poincaré map sampling that uses two quality measures to enforce this property.

First, we impose an upper bound on the range of winding values present in a cell, *i.e.*,

$$\Delta \mathbf{W}_c = \mathbf{W}_{\max \forall v} - \mathbf{W}_{\min \forall v} \leq \boldsymbol{\Psi}_w, \quad (16)$$

where $v \in [1, 4]$ designates the cell vertices, and $\boldsymbol{\Psi}_w$ is a user-defined parameter. The values of $\boldsymbol{\Psi}_w$ bound the dynamic range within a cell, so smaller values yield smaller analysis cells during the subdivision process. Our second control measure aims to ascertain the local quasi-linearity of the winding numbers variations. If \mathbf{W}_i represents a winding number set for a Poincaré section point (with index i) inside a particular analysis cell, then all n internal points to a cell should satisfy

$$\mathbf{W}_{\min \forall c} - \boldsymbol{\epsilon}_w \odot \boldsymbol{\Psi}_w \leq \mathbf{W}_i \leq \mathbf{W}_{\max \forall c} + \boldsymbol{\epsilon}_w \odot \boldsymbol{\Psi}_w. \quad (17)$$

$\boldsymbol{\epsilon}_w$ is another set of user-specified parameters, and the \odot symbol represents element-by-element multiplication of vectors ($\mathbf{a} \odot \mathbf{b} = (a_1 b_1, a_2 b_2, a_3 b_3)$). Any cell that fails the criteria in either Equation 16 or Equation 17 encompasses too much dynamical behavior or surrounds a spatially diverse dynamical region, and is marked for subdivision.

Practically, we use a multiresolution mesh data structure that allows us to record winding numbers both at the sampling vertices and inside the cells. Since all Poincaré section crossings of a given trajectory share the same winding numbers \mathbf{W} set as the initial vertex, each one of the $p - 1$ returns, or $\mathcal{P}^q(\mathbf{x})$, $q \in [1, p - 1]$, is assigned the same \mathbf{W} values. These values are added to the cell containing the return and are then tested as part of the subdivision criteria in Equation (17). When required, cells are regularly subdivided with internal data assigned to the corresponding quadrant within the original cell. A user-specified maximum depth level parameter, d_{\max} , is employed to represent the total number of subdivision layers allowed. For example, a $d_{\max} = 3$ specifies that an initial analysis cell at $d = 0$ can produce up to 64 subcells. Cells are also subdivided if any corners reside within invalid dynamical regions.

To illustrate the benefits of this technique, we show in Figure 3 the adaptive resolution mesh produced in the domain D_{EM} for a maximum refinement depth $d = 3$. The initial grid is shown in thick gray lines. The highest resolution is achieved in chaotic regions where the dynamics is most complex. This result is in fact excellent from an astrodynamics perspective since the saddles embedded in chaos offer the most versatile transfer opportunities. Regions of regular dynamics, in contrast, are coarsely resolved, as expected.

5.2 Poincaré section transversality

An issue that frequently prevents the computation of the Poincaré index in existing techniques is the presence of discontinuity of the Δ mapping along cell edges. Two properties of the CR3BP can explain this behavior: highly sensitive dynamics and transversality violation of the flow map for the chosen section Σ .

Transversality violations are typically the result of one of two specific trajectory events. First, trajectories that are tangent to the section along their path generate discontinuities in Δ , see Figure 5.2. A second

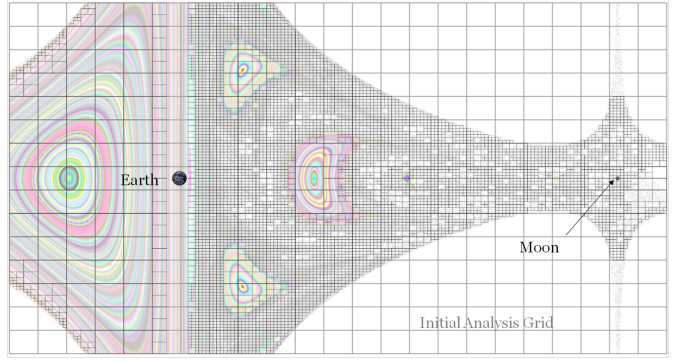


Fig. 3. Adaptive cell subdivision based on the winding number set \mathbf{W} applied to the domain D_{EM} with parameters $C = 2.96$ and $d_{\max} = 3$.

event is an exact intersection by the trajectory of a singularity in the model such as the primaries in CR3BP (exemplified in Figure 5.2).

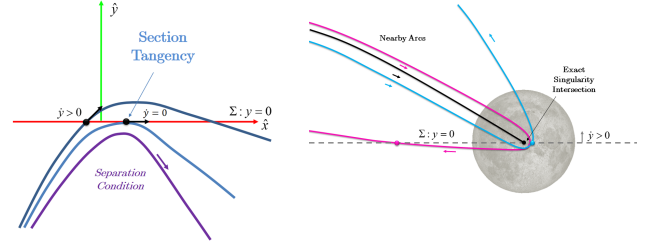


Fig. 4. Transversality violation types in the CR3BP. Left: section tangency, Right: singularity intersection.

5.3 Resolving the Poincaré Index

We perform the evaluation of the Poincaré index in non-transverse cells by considering the behavior of Δ in the limit approaching a transversality violation. A discontinuity of Δ at some location \mathbf{g} on the closed curve Γ for period p creates a discontinuity in the Poincaré index at \mathbf{g} . However, since the limits of the angular coordinate $\alpha(\Delta(\mathbf{g}))$ exist in various directions approaching \mathbf{g} , the Poincaré index can be expressed as the summation of improper integrals

$$\kappa = \frac{1}{2\pi} \oint_{\Gamma} d\alpha(\Delta) = \frac{1}{2\pi} \left(\int_{\boldsymbol{\gamma}_0}^{\mathbf{g}} d\alpha(\Delta) + \int_{\mathbf{g}}^{\boldsymbol{\gamma}_0} d\alpha(\Delta) \right), \quad (18)$$

where $\boldsymbol{\gamma}_0$ is a starting point along Γ ($\boldsymbol{\gamma}_0 \neq \mathbf{g}$).

The adaptive edge sampling approach already used in prior work [13] is augmented with additional heuristics to detect transversality violations. Subsequent map states along cell edges are tested for transversality violations via a set of heuristic trials that search for fundamental differences in map information. The adaptive subdivision of an edge localizes the locations of \mathbf{g} and generates sufficient approximations of the limiting values of $\alpha(\Delta(\mathbf{g}))$. Luckily, all information required for heuristic detection is available during numerical simulation or easily retrieved from the output. It should be noted that transversality violations tend to form coherent contours on the section domain that represent fundamental transitions between trajectory types. This allows us to heuristically detect the two types of transversality violations and resolve the Poincaré index using a piecewise integral.

5.4 Fixed Point Refinement

The computation process to extract fixed points as described by Tricocche et al. [17] was reinforced with shooting schemes [13] to accommodate the sensitive dynamics associated with corrections procedures in multi-body problems.

Yet, the single shooting and multiple shooting solutions used in prior work are only moderately successful at finding fixed points because each differential corrections technique possesses varying convergence properties and will often fail to find a fixed point. To remedy this situation, we apply differential corrections procedures in a predefined sequence chosen to maximize the convergence basin of the fixed point. Practically, we start with single shooting refinement, and switch to the variable-time multiple shooting method if this first attempt fails. If both solutions fail, we apply a quasi-Newton single shooting method, which is significantly more expensive than the previous two but possesses stronger convergence properties.

5.5 Determining the Initial Guess for Fixed Points

Irrespective of the chosen refinement procedure, the refinement result is still heavily contingent on the quality of the initial guess. Our solution starts by sampling Δ at a set of regularly distributed positions within the cell. Instead of working directly with Δ , however, we consider the map tangent $\eta(\mathbf{x})$ instead, defined as

$$\eta(\mathbf{x}) = \mathcal{P}^p(\mathbf{x}) - \mathcal{P}^{-p}(\mathbf{x}), \quad (19)$$

which can be seen as a low-pass filtering that cancels out the dominance of the unstable mode in the vicinity of a saddle-type¹ fixed point [14, 9]. Practically, if the considered variable is $\zeta = \mathbf{x} - \mathbf{s}$ with \mathbf{s} representing the saddle-type fixed point location, then a quadratic model of the sampled dynamic is formed as

$$\dot{\zeta} = A_s \zeta + \frac{1}{2} \zeta^T \underline{Q} \zeta. \quad (20)$$

Note, A_s is a 2×2 matrix, and \underline{Q} is a $2 \times 2 \times 2$ tensor where $\underline{Q} = 0$ in the linear model. A Levenberg-Marquardt optimization process is applied to fit the model to the sampled data [11] and infer the approximate location of the fixed point.

Unfortunately, the model-fitting strategy outlined above cannot be applied in cells containing transversality violations. In such cases we apply a different approach, namely we identify the position along each edge of the cell where the norm $|\Delta|$ is minimal and then sample this same quantity along the 6 possible lines that connect these 4 minima, seeking the minimal norm inside the cell. The motivation for this approach stems from the fact that one these lines should closely match the stable manifold of a saddle-type fixed point.

5.6 Invariant Manifold Extraction

Eigenanalysis of the full-period STM (or monodromy matrix \mathcal{M} in Equation (10)) allows us to determine the stability type (saddle or center) of each discovered fixed point (Equation 11). If a saddle type is identified, the construction of the invariant (stable and unstable) manifolds constitutes the last step of the topology extraction and we derive eigenvectors and stability index (Equation 13) from \mathcal{M} .

Prior work [17, 13] directly applied to the construction of invariant manifolds a method proposed by England *et al.* [4], which proceeds through a series of two-point boundary problems that aim to ensure smoothness and fine sampling of the manifold. Unfortunately, this solution does not handle the issue raised by transversality violations in the CR3BP, nor does it provide any guidance to accommodate the numerical challenges associated with this particular system. We describe in the following our improvements of this method.

Manifold Extraction with Curve-Refinement. Consider two adjacent positions ϕ_i and ϕ_{i+1} that form a segment $w = \overline{\phi_i \phi_{i+1}}$ on the manifold. We further assume that both positions are close enough such that linear interpolation between these two positions yields positions that are themselves on the manifold. Applying the Poincaré map \mathcal{P}^p to any such intermediate position will result in a new position further downstream on the manifold. Refer to Fig. 5 (top). The basic idea of the algorithm by England *et al.* [4] is that adaptive sampling of the segment w by the Poincaré map, controlled by curve quality checks,

¹Saddles are far more challenging to extract than centers and much more likely to explain situations of failed convergence

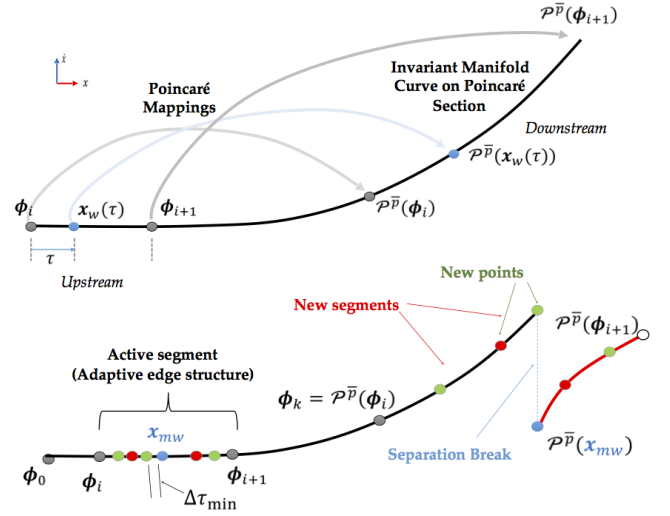


Fig. 5. Top: Schematic of a 1D invariant manifold curve on the Poincaré section. Bottom: Generating new downstream manifold points and segments through a transversality violation.

allows one to construct the next segment $= \overline{\phi_{i+1} \phi_{i+2}}$ on the manifold and ultimately extract the entire manifold by repeating this operation, see Fig. 5. Our solution follows the same approach while simultaneously checks for Poincaré map discontinuities along the way, thereby explicitly handling transversality violations.

The heuristics for detecting transversality violations during Poincaré index evaluation are reapplied alongside the curve-refinement criteria. If a downstream transversality violation is detected between consecutive segment samples, the segment is bisected on that interval. Subdivision continues until the distance between consecutive points reaches a user-prescribed minimal distance (u_{\min} , which corresponds to a relative distance $\Delta\tau_{\min}$). An example is depicted in Figure 5 (bottom) where downstream mappings are color-coded by their initial position on the active segment: a downstream transversality violation exists between ϕ_i and the midpoint x_{mw} , and subdivision localizes the separation condition when the parameter differential is below $\Delta\tau_{\min}$.

Seeding an Invariant Manifold on the Poincaré Section. A small step away from a fixed point along an appropriate eigenvector direction approximates an initial state on the invariant manifold; yet, the step along the eigenvector creates a perturbation in all 4 dimensions of the CR3BP. Unfortunately, direct projection of the eigenvector onto the hyperplane Σ yields a vector that inadequately characterizes the on-section manifold curve. Consider the example of the 4D step from a fixed point (\mathbf{x}^* defined on the hyperplane Σ) onto the eigenvector \mathbf{v}^{S+} . The on-section normalized representation of the same invariant manifold space, defined as $\mathbf{u}^{U/S}$, is then created by propagating $\mathbf{x}^* \pm \epsilon_N \mathbf{v}^{U/S}$ to the nearest crossing of Σ . $\mathbf{u}^{U/S}$ represents the correct eigenvector projection onto section coordinates and our algorithm begins by taking a small step onto this projection.

Stopping Criteria. While the initial manifold construction method [4] used a simple limit on the total arc length to stop the progression of the algorithm, more recent work has shown that manifolds encounter other saddle points in the same island chain, a case that is prevalent in the CR3BP. Practically, we found two criteria primarily effective in controlling the length of a manifold.

The first stopping criteria tracks a practical measure for spacecraft trajectory planning. We saw previously that the manifold construction algorithm essentially maps upstream segments to downstream segments, thereby creating a parent-child relationship between them (see also discussion in Sect. 6.3). Our algorithm caps the manifold progression by stopping when the depth of this relationship reaches a maximum depth $d_{w,\max} = 5$.

The second stopping condition observes simultaneous advection of manifolds from the same periodic orbit for the detection of saddle-loops. Newly-generated downstream segments from both the stable and unstable manifolds of the *same periodic orbit* are compared to detect if a segment crossing occurred.

Screening Computations Given the high computational cost of manifold construction, and in the interest of efficiency, we perform several tests beforehand to prevent unnecessary computations.

An effective way to accelerate the extraction of manifolds is to pre-screen for potentially impractical structures for spaceflight, *i.e.*, periodic orbits with exceptionally high instabilities. A threshold cutoff is established on stability index magnitude at $|v_{SJ}| > 10^6$ (refer to Equation 12) for manifold extraction. In addition, more screening (or a lower $|v_{SJ}|$ cutoff) reduces the overall workload required by PMATE and is often implemented in practice. Suggested thresholds are listed in Table 1.

A second important observation is that a lower bound is necessary for u_{\min} (which regulates upstream manifold segment subdivisions) as a transfer stipulation for realistic spaceflight. Error in real-world devices such as sensors and engines translate into limitations on state acquisition and deliverable maneuvers; if a particular transfer requires that the position and velocity match a desired state to 10^{-6} m and 10^{-6} m/s, for example, that trajectory may not be flight worthy as many instruments cannot deliver that level of accuracy [19, 5]. Spacecraft state determination outside of low Earth orbits is limited to an accuracy of 3 km for position and 0.1 mm/s for velocity based on measurement error of standard capabilities [21]. Practically, we require u_{\min} values above 2×10^{-5} (nondimensional map displacement) for the Earth-Moon system, which is equivalent to 2.05 cm/s for velocity and 7.69 km for position. Note that the value of u_{\min} is different across CR3BP systems. Refer to Table 1 for suggested values.

System	u_{\min}	Δ_{\min}	Δ_{\max}	α_{\max}	$(\Delta\alpha)_{\max}$	$ v_{SJ} _{\max}$
EM	2×10^{-5}	1×10^{-5}	0.1	0.3 (17.2°)	0.001	2.5×10^3
ST	4×10^{-6}	1×10^{-6}	0.05	0.1 (5.7°)	0.001	2.5×10^3
SEnc	1×10^{-6}	1×10^{-6}	0.05	0.1 (5.7°)	0.001	5.0×10^3

Table 1. Heuristic parameters employed for invariant manifold advection in the indicated CR3BP systems. Phase space displacement values are listed in nondimensional units.

6 APPLICATIONS TO ASTRODYNAMICS

Periodic orbits and associated invariant manifolds supply a rich dynamical knowledge that is essential for a versatile spaceflight design platform. As shown in the following, interactive selection of arcs and design node links broadens the design possibilities with new options and the ability to quickly examine trade-space decisions.

6.1 Analysis of Novel Periodic Orbits

Our fixed point extraction easily locates periodic orbits that are found through conventional analysis (*e.g.*, members of the Lyapunov and resonant orbit families). In addition, our method reveals many periodic orbits that are either challenging to discover with traditional analysis in general, or previously unknown.

Earth-Moon System. At a Jacobi constant level of $C = 3.2$, the closed L_1 and L_2 gateways prohibit flow between the primaries, yet chaos is still present. Our results, displayed in Figure 6, reveal saddles and centers grouped in island chains and saddle-type fixed points within the limited chaotic regions. The periodic orbits in Figure 6 are displayed in the xy plane (x -axis in red, y -axis in green). In Figure 6 and subsequent images, fixed points belonging to the same periodic orbit are marked with the same color. At $C = 3.2$, transversality violations are rare within the analysis domain since the chaos is bounded, and the fixed point extraction is relatively straightforward with little use for cell subdivision.

A more complex yet practically relevant case resides at an energy level where chaos exists throughout the planar flow space. The Earth-Moon system with $C = 2.96$ permits trajectories everywhere in the xy

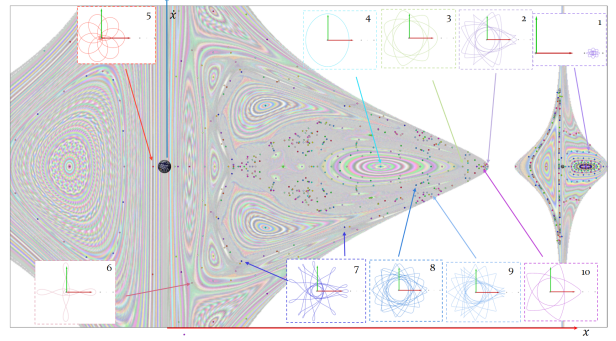


Fig. 6. Fixed points and selected periodic orbits found in the Earth-Moon system at $C = 3.2$.

plane. Broader sampling parameters are applied over a larger analysis domain (see Trial 1 in Table 2). We obtain a set of fixed points throughout D_{EM} with sparse behavior capture near lunar vicinity. Therefore, a more refined extraction is performed near the Moon. Refer to Trials 2, 3, and 4 in Table 2. As shown in Figure 1, the fixed points extracted for $C = 2.96$ in the EM system are numerous, reaching a total of 1450 distinct periodic orbits.

Trial	C	Domain (x, \dot{x}) (nondim)	Resolution	l_{\min}	p_{\max}
0	3.2	$[0.4, 1.1] \times [-2.5, 2.5]$	24×16	8×10^{-5}	12
1	2.96	$[0.4, 1.1] \times [-2.5, 2.5]$	24×16	8×10^{-5}	12
2	2.96	$[0.9, 1.0] \times [-1.5, 1.5]$	8×8	2×10^{-5}	12
3	2.96	$[0.78, 0.92] \times [-0.4, 0.4]$	8×8	2×10^{-5}	6
4	2.96	$[0.9925, 1.08] \times [-0.2, 0.2]$	6×6	2×10^{-5}	4

Table 2. Parameters used in the Earth-Moon system.

The identified periodic orbits are then inserted in a large data base, along with their integral period, stability type, $|v_{SJ}|$, spatial coordinates as well as overall time period. The corresponding Orbit IDs are listed on the sample orbits shown in Figure 1 for easy reference during sample design scenarios.

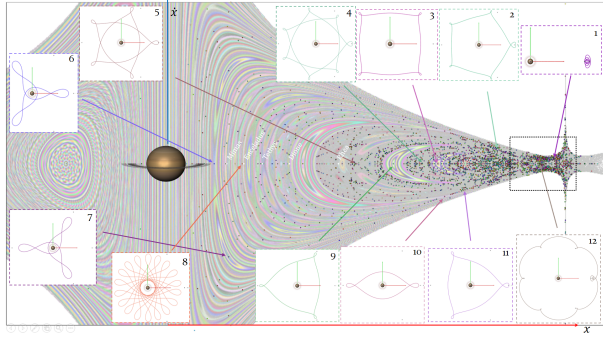
Among the fixed points found at $C = 2.96$, many novel saddle-type periodic orbits were identified. As shown in Figure 1, several periodic orbits are commonly known such as Orbit 4 (the L_1 Lyapunov), Orbit 23 (1:2 resonant orbit), Orbit 49 (stable 3:2 resonant orbit), Orbit 51 (unstable 3:2 resonant orbit), and Orbit 50 (the $p = 3$ unstable DRO - quasi-periodic island near the Moon) [16, 3, 1]. Several orbits, though, transit between the interior and exterior regions (such as Orbit 1433) and DRO vicinity to exterior or interior (Orbits 229, 826, and 1357). Yet others like Orbit 1439 visit all the aforementioned regions, perhaps making such orbits potentially useful for transfer design. And though the analysis is only performed within the primary analysis domain D_{EM} on the $\Sigma : y = 0$ Poincaré section (as per Table 2) an abundant number of unstable periodic orbits that cross this section travel to L_3 , L_4 , and L_5 vicinities. Clearly, our results offer a vivid dynamical understanding of this particular system.

6.1.1 Saturn-Titan System

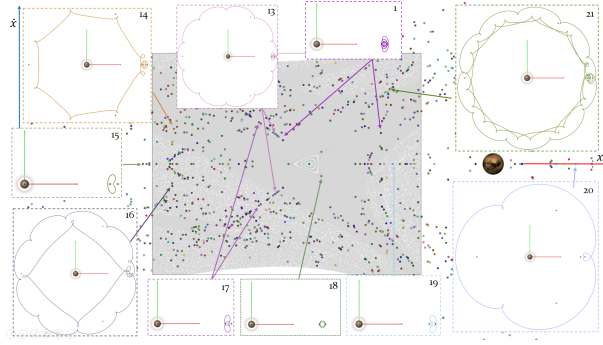
Employing a primary analysis domain similar to D_{EM} with supporting refined domains (see Table 3), our method discovers 845 distinct periodic orbits ranging up to period $p = 12$ at $C = 3.00$ in the Saturn-Titan system. These periodic orbits, shown in Figure 7, encompass the more traditional orbits and several periodic paths that transition between various regions. Orbits in the vicinity of the DRO (Figure 7(b)) may hover around Titan, transit to the interior or exterior, or visit multiple areas of phase space up to a limit in the interior. The crossing locations of the inner-moon orbits are also indicated in Figure 7(a). At this particular energy level, saddle-type periodic orbits reside in fairly close proximity to the listed interior Saturnian moons, but manifold extraction is necessary to determine if any low-cost transfers from either the Saturn-Titan exterior or Titan vicinity to such orbits exist.

Trial	C	Domain (x, \dot{x}) (nondim)	Resolution	l_{\min}	p_{\max}
0	3.00	$[-0.4, 1.1] \times [-2.5, 2.5]$	24×16	8×10^{-5}	12
1	3.00	$[0.932, 0.986] \times [-0.136, 0.136]$	8×8	2×10^{-5}	6
2	3.00	$[0.98, 1.05] \times [-0.225, 0.225]$	10×10	2×10^{-5}	6

Table 3. Parameters used in the Saturn-Titan system.



(a) Primary analysis domain



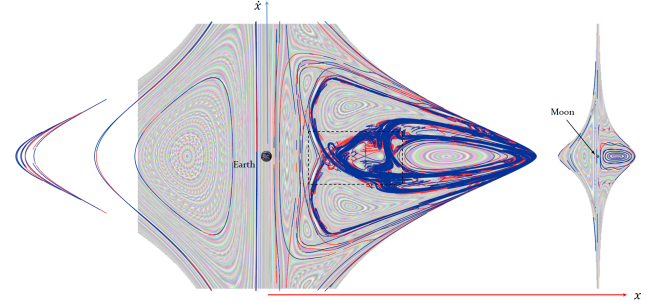
(b) Area near DRO

Fig. 7. Fixed points available at $C = 3.00$ in the Saturn-Titan system. This is the collective result for the trials in Table 3.

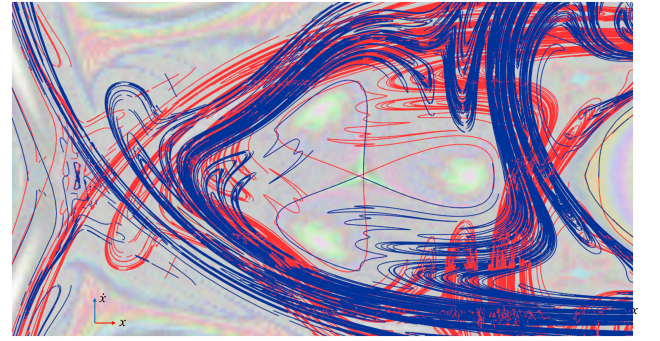
6.2 Poincaré Map Topology Structure

With fixed points extracted, the complete Poincaré map topology structure is characterized by means of our invariant manifold extraction algorithm, which is first demonstrated in the Earth-Moon system at $C = 3.2$. The large-scale topology extraction result appears in Figure 8 with unstable manifolds (W^U) and stable manifolds (W^S) colored in red and blue, respectively. At $C = 3.2$, invariant manifolds are extracted throughout the chaotic areas, thoroughly filling in the phase space areas between quasi-periodic islands. Our algorithm captures saddle-center island chains except on some islands near the Moon. Difficulties near the Moon can be explained by numerical sensitivity and numerical error build-up during integration as trajectories pass exceptionally close to the singularity multiple times before completing the \bar{p} -th iterate. As with fixed point extraction, advecting invariant manifolds for the Earth-Moon system at $C = 3.2$ is not as challenging as at other Jacobi constant values since fewer hyperplane transversality violations are encountered. In fact, this manifold set is processed without stability index pre-screening and still completes the advection procedure faster than systems with open gateways. Yet, some challenges in describing the Poincaré map topology skeleton are visible in a close-up representation (Figure 8(b)). Artifact segments shortcut some tight bends in both manifold types, but these are merely caused by loose curve-refinement parameters. Chaotic tangles, on the other hand, strongly influence the generation of invariant manifolds, especially as a manifold is advected towards the origin fixed point of the opposing stability type. As evidenced by the tri-lobe structure in Figure 8(b), it is unclear if the computed structure is a pure saddle-loop (a completely connected tri-petal flower) or if the chaotic tangle oscilla-

tions in the manifold are the true projection of the invariant manifold streamsurface. Nevertheless, the computed topology skeleton is still an applicable representation of manifold behavior for design practices.



(a) Primary analysis domain D_{EM}



(b) Zoom-in on indicated domain

Fig. 8. The Poincaré map topology skeleton (W^U in red and W^S in blue) computed with the manifold extraction algorithm in the Earth-Moon system within the domain D_{EM} at $C = 3.2$.

The Poincaré map topology is next extracted on a section with open gateways. At $C = 2.96$ in the Earth-Moon system, advection produces a depiction of both stable (blue) and unstable (red) manifolds for the periodic orbits shown in Figure 9. Individual stable and unstable manifold skeletons appear in Figures 10(a) and 10(b), respectively. Limits on base orbit stability index ($|v_{SI}| \leq 2500$) screen considered fixed points to reduce overall computation during the advection procedure, cutting in half the number of saddle-type orbits included. Even with a selective range on v_{SI} , the advected set of manifolds populate almost the entire chaotic region. As shown by the W^S portrait in Figure 10(a), the only areas within the chaotic sea without stable manifolds are associated with trajectories that escape the entire Earth-Moon system. Knowing this highly detailed stable manifold structure, a spacecraft in almost any location within the applicable chaotic sea can reach a stable manifold of some fixed point with a small ΔV . This rich understanding of the available flow is extremely beneficial to spaceflight applications as nearby paths to almost any Poincaré section state are revealed.

In the Saturn-Titan system, the manifold advection algorithm produces results similar to the Earth-Moon system at $C = 2.96$ with open gateways. Invariant manifolds are displayed in the Saturn-Titan system at $C = 3.00$ below in Figure 11. Again, limits on considered periodic orbits via stability index prevent tedious advection. A depiction of stable manifolds and fixed points in Titan-vicinity appears in Figure 6.2. Once more, the invariant manifolds create a comprehensive skeleton in the chaotic zones. The dense structures near Titan offer many options for heteroclinic transition between periodic orbits. The inner moons Mimas, Enceladus, Tethys, Rhea, and Dione are also

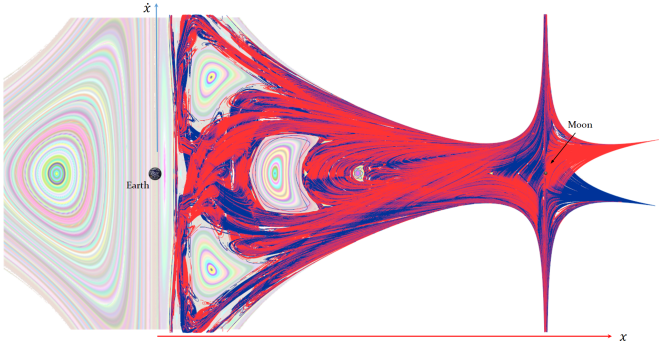


Fig. 9. The Poincaré map topology skeleton (W^U in red and W^S in blue) computed in the Earth-Moon system at $C = 2.96$.

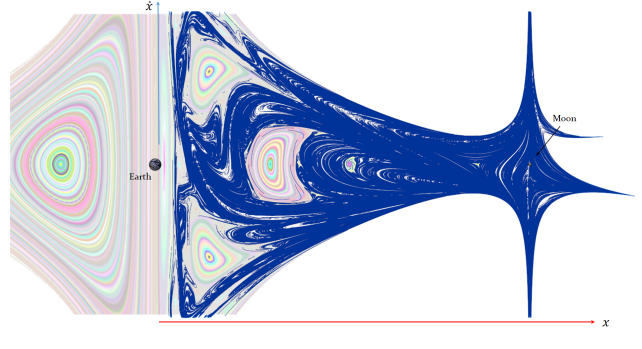
added to Figure 11 as white dots. Clearly, Rhea and Dione are accessible at this energy level with a multitude of invariant manifold structure of the Saturn-Titan system intersecting the indicated positions. Yet, the other interior moons are only accessible with a saddle in bounded chaos, meaning a substantial maneuver ($\Delta V > 500$ m/s) is necessary for a spacecraft to cross over the multiple layers of bounded dynamics. Saddle-center island chains outline the dynamical boundaries of the problem towards the inner moons like Tethys and Enceladus and could be useful for design practices. The natural dynamics pathway to the inner moons, however, should employ the gravity fields of other moons like Rhea and Dione to assist a spacecraft over the regions of bounded dynamics in the Saturn-Titan system. Here, the Poincaré map topology skeleton in the CR3BP provides alternative pathways to initialize or finalize a moon-tour trajectory.

6.3 Extracting Discrete Arcs on Invariant Manifolds

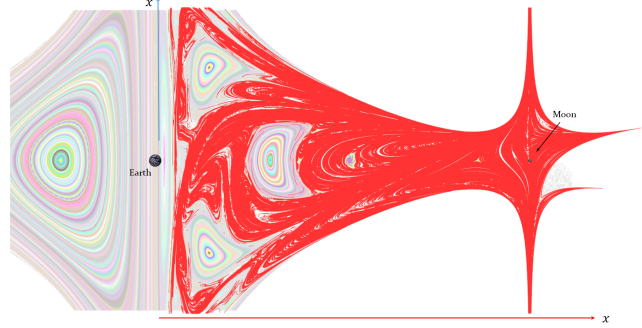
Exploiting Poincaré map topology for design purposes requires the ability to access any arbitrarily selected state on an invariant manifold. The goal is either to reconstruct the *upstream* pathway to a current selection point or the *downstream* pathway beyond the selection state. Constructing the downstream destination of a selection point is simply a downstream integration of the dynamics from the selected point. Upstream propagation, on the other hand, defines how the trajectory progresses from the base periodic orbit downstream to arrive at the selected manifold state. In either case, a discrete arc at a user-selected invariant manifold state is extracted by first isolating which manifold and segment correlates with a user selected location from the visualization. Recall that our algorithm constructs invariant manifolds on a Poincaré section as a series of linear segments connecting adjacent map states (ϕ_i). Given the highly sensitive nature of the state selection process, the low-precision selection in image coordinates is mapped to a double precision selection via a hash table. Converting the line segment selection within the visualization to a manifold segment then yields the source manifold and the originating periodic orbit for additional arc-extraction procedures.

Even with the user-selected invariant manifold state, additional adjustments are necessary to reproduce the upstream pathway of the selected state. Indeed, propagation of the extracted state $\mathbf{x}_c(u)$ upstream is bound to fail due to the repelling action of the manifold on the neighboring flow [8].

Upstream manifold arc reconstruction circumvents the aforementioned challenges thanks to a data structure constructed by our manifold advection procedure. The algorithm advects states sampled from an upstream manifold segment to create a group of new downstream segments thereby linking upstream segments as the parents of spawned downstream segments (or child segments). This parent-child relationship among segments allows for the organization of segment data into a *manifold segment tree*. To illustrate, sample manifold segments near the start of the advection procedure are arranged as a staircase schematic indicating depth levels (d_w) in Figure 12; each step down



(a) Stable manifolds



(b) Unstable manifolds

Fig. 10. Stable and unstable manifolds on the Earth-Moon system domain D_{EM} at $C = 2.96$.

symbolizes the downstream progression to the next group of segments at after \bar{p} map iterates.

The manifold segment tree links an arbitrarily selected manifold state ($\mathbf{x}_c(u)$) on a known manifold segment back to the initial manifold segment to trace out the upstream arc. Let us consider a user-selected child segment (c) and the corresponding parent segment w . The parameter τ identifies a position on the parent segment, and the values τ_0 and τ_1 locate the segment w states $\mathbf{x}_w(\tau_0)$ and $\mathbf{x}_w(\tau_1)$, respectively. The mappings of $\mathbf{x}_w(\tau_0)$ and $\mathbf{x}_w(\tau_1)$ are previously employed by manifold advection procedures to produce the endpoints of Segment c . Since the user-selected point $\mathbf{x}_c(u)$ resides between ϕ_k and ϕ_{k+1} , a corresponding initial state exists on the parent segment between $\mathbf{x}_w(\tau_0)$ and $\mathbf{x}_w(\tau_1)$ that maps downstream to $\mathbf{x}_c(u)$. Let $\mathbf{x}_w(\tau_u)$ represent the upstream mapping of $\mathbf{x}_c(u)$ such that the linear parameter τ_u locates $\mathbf{x}_w(\tau_u)$ on Segment w ($\tau_0 \leq \tau_u \leq \tau_1$). If the parent τ value, or source value, is stored with every manifold point, then the upstream mapping of the user-selected state $\mathbf{x}_c(u)$ can be extracted for a single tree-depth level ($-\bar{p}$ iterates) by linear interpolation between $\mathbf{x}_w(\tau_0)$ and $\mathbf{x}_w(\tau_1)$. Reconstructing the full set of upstream nodes to Segment 0 is achieved by repeating this procedure. Thus, the upstream pathway is formed *without* numerical integration, which is extremely powerful for interactive analysis. A similar procedure can also be implemented to reconstruct iterates downstream of a selection if downstream nodes exist in the manifold segment tree.

Tracking Relevant Quantities. The manifold tree used to organize the manifold information is also applied to store different quantities along the invariant manifold. Quantities that are relevant to a design of interest, including closest approach to a singularity and time of flight are already considered during the advection algorithm to heuristically test for transversality violations; storing this design data within the manifold segment tree permits the quick retrieval of transfer information without actually evaluating the entire manifold trajectory through propagation. Tracked information greatly assists the interactive de-

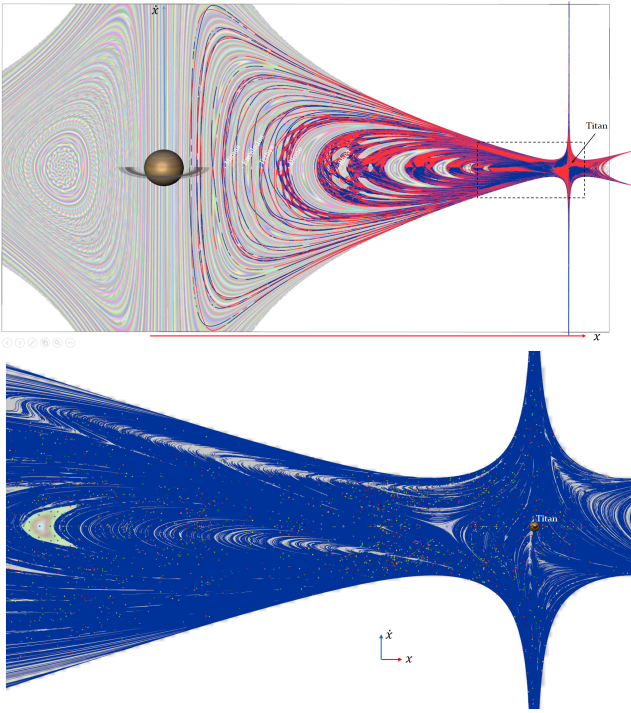


Fig. 11. The Poincaré map topology skeleton (W^U in red and W^S in blue) in the Saturn-Titan system at $C = 3.00$.

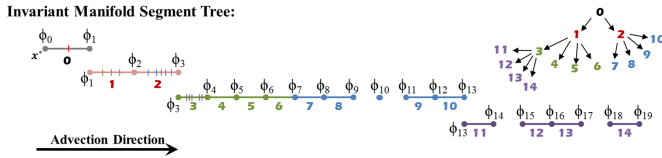


Fig. 12. As the invariant manifolds are progressed via curve-refinement, the spawning of new manifold segments generates a tree structure that can be employed for accessing data.

sign process as designers examine the trade space of available arcs for a minimal transfer flight time or for invalid transfers that get too close to a celestial body.

Interactive Definition of Heteroclinic and Homoclinic Connections. With the capability to reconstruct an upstream arc from an arbitrary manifold state, the extraction of heteroclinic (\mathcal{H}_c) and homoclinic (\mathcal{H}_o) connections is now a trivial matter. If the point selection coincide with *both* a stable and an unstable invariant manifold, the point represents a discrete trajectory connection between the two manifold types as well as a natural pathway between the two base periodic orbits. Time of flight for the whole connection is collected as the summed contribution of the two arcs back upstream to Segment 0 without propagation. The approximated time of flight for a selected transfer can be easily shown as text next to the green connection point. Numerous free-connection possibilities exist between saddle-type orbits, but the ability to examine data allows a designer to quickly search for a superior option.

6.3.1 Defining Practical Arrival (or Departure) Points

A practical entrance point (or departure point) is established for manifold arcs and connections. With upstream arc reconstruction, tracing a user-selected manifold arc closer to the root segment generates a geometry that appears like many revolutions of the periodic orbit. Upstream arcs near the highest segments in the manifold segment tree are *not* revolutions of the periodic orbit by definition; however,

the upstream portions do closely resemble the periodic orbit. Even though the spacecraft is still on the invariant manifold in transit, the asymptotic approach path closely mimics the intended periodic orbit such that operations and scientific measurements may start long before reaching the manifold termination segment (Segment 0 upstream).

Thus, the orbit arrival (or departure) point for an invariant manifold arc is achieved when the downstream manifold position surpasses a given distance δ_W away from the closest position on the corresponding periodic orbit. Geometric similarity considers the entire numerically simulated pathway, so this practical orbit arrival (or departure) process should only be applied after a design is crafted. In the Earth-Moon system, the value of δ_W is selected as 8000 km for weak-strength manifolds and 1000 km otherwise. Different CR3BP systems require adjustments to δ_W to accommodate the modified dynamics.

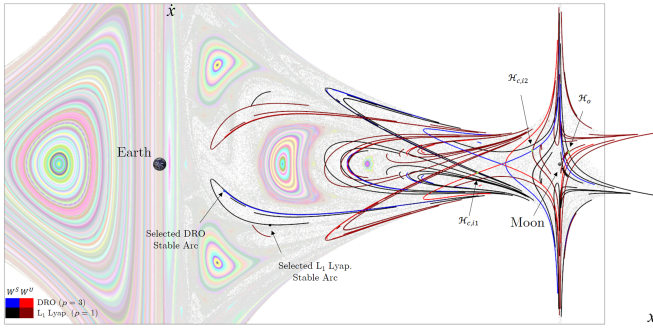
6.4 Design Elements of Poincaré Map Topology in the Earth-Moon System

Manifold arc selection offers a key tool for design construction with Poincaré map topology. Consider the smaller topology skeleton subset that includes just the invariant manifolds of the L_1 Lyapunov and the $p = 3$ unstable DRO, see Figure 13. The subsample of manifolds appears on the Poincaré section with the W^S and W^U pair colored with black and crimson for the L_1 Lyapunov and with blue and red for the $p = 3$ DRO, respectively. A L_1 Lyapunov stable manifold arc (black) and a $p = 3$ DRO stable manifold arc (blue) are selected at the indicated locations on the Poincaré section (Figure 13(a)) that originate in the interior region. Both resulting arcs (shown in the rotating frame in Figure 13(b) and in the inertial frame in Figure 13(c)) demonstrate an elliptical orbit around the Earth before a second passage where the CR3BP dynamics shift the trajectories towards asymptotic approach of the respective orbits. The time of flight of the transfer trajectory considers the propagation time from the initial selection point until the geometric similarity condition between the manifold and desired orbit (see Section 6.3.1). The black arc enters the L_1 Lyapunov orbit at the practical arrival condition after 38.10 days whereas the blue arc practically arrives in the $p = 3$ DRO after 88.14 days. Clearly, the arc selection capability enhances quick design construction by readily incorporating many ballistic capture trajectories.

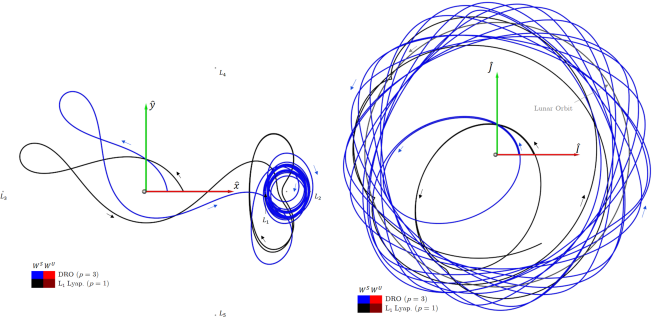
6.5 Sample Connections Between Saddle-type Orbits

Heteroclinic and homoclinic connections between the L_1 Lyapunov orbit and the $p = 3$ DRO are quite simple to extract from Poincaré map topology with manifold selection capabilities. Any intersection of stable and unstable manifolds offers a pathway between their respective fixed point, so a multitude of options exist to exploit natural dynamics to transfer between the two orbits. Also apparent in Figure 13(a) are green points that signify selected heteroclinic connections between the $p = 3$ DRO and L_1 Lyapunov orbit in the interior region ($\mathcal{H}_{c,i1}$ and $\mathcal{H}_{c,i1}$) and the exterior region ($\mathcal{H}_{c,e1}$ and $\mathcal{H}_{c,e1}$). A homoclinic connection for the L_1 Lyapunov orbit also appears in Figure 13(a) as the point \mathcal{H}_o at the intersection of a crimson W^U and a black W^S . The chosen interior connection arcs are displayed in Figure 14 while the exterior connections appear in Figure 15. The simplicity of formulating free-flowing connections between unstable periodic orbits assists designers in evaluating different trade studies to align timing possibilities.

Additional connections are also easy to formulate between a wide variety of periodic orbits. An interesting transfer is demonstrated starting at the $p = 3$ DRO and departing to the rather exotic orbit that visits L_3 and L_4 vicinities while also closely approaching the Moon several times. We refer to this orbit as *Orbit O^** in the following. The invariant manifold curves of that orbit (displayed in Figure 16 with indigo and tan colors) indicate that a lot of Poincaré section locations naturally flow into this orbit with the large dispersion of stable manifolds. A transfer from the $p = 3$ DRO to this orbit is represented by any red-indigo intersection, and a selected option demonstrates a transfer possibility as shown in Figure 16(b). The richness of PMATE manifold information combined with the ability to construct heteroclinic connections with ease highlights essential orbits for use as



(a) Manifolds of the L_1 Lyapunov and $p = 3$ DRO periodic orbits



(b) Selected arcs (rotating frame) (c) Selected arcs (inertial frame)

Fig. 13. Invariant manifolds for the L_1 Lyapunov and $p = 3$ DRO saddle-type orbits extracted with PMATE in the Earth-Moon system ($C = 2.96$). Selected stable manifold arcs are displayed in the rotating (b) and inertial (c) frames.

intermediate transfer candidates with a high degree of transfer centrality as indicated through manifold dispersion.

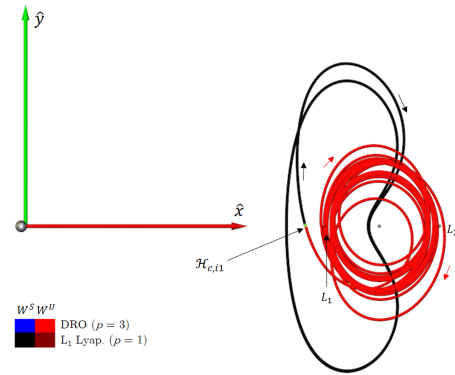
7 CONCLUSION

We have presented an algorithmic solution that enables the automatic extraction of the topology in the circular restricted three body problem, specifically periodic orbits and associated invariant manifolds. In particular, we have discussed the challenges that are specific to this type of system and proposed a range of improvements over existing methods to address them.

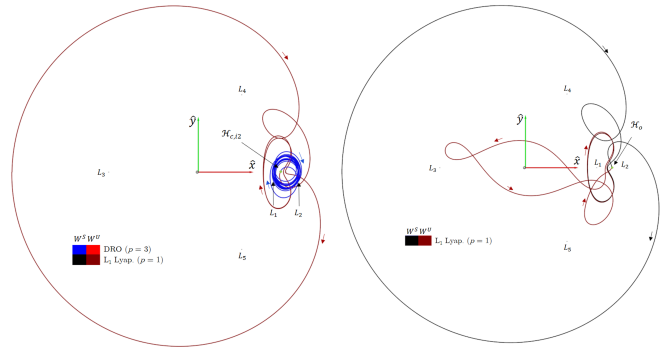
As we have shown, our method exposes the connectivity of orbital structures, which offers spacecraft trajectory designer a broad range of options without external computation. Our experimentation with this approach suggests that a designer could employ automated topological skeletons as an input catalog to select pathways that navigate the available dynamical flow. By selecting stable and unstable manifolds of various fixed points that are available on a Poincaré map, low-cost transfers are simply traced through the stable-unstable manifold network since all of the relevant orbital data is automatically generated as part of the process. With our proposed manifold construction, linear intersections tests for the numerous segments of the manifolds can autonomously deliver the ΔV -free connections between periodic orbits for additional design options during path planning. In the future, a logical step towards limiting computation exists, namely finding periodic orbits that are central to the problem, driving the underlying topology. Restricting the visual analysis to just those central orbits could greatly reduce the computational effort, but a function to determine orbit centrality is still an open problem.

REFERENCES

[1] L. Capdevila. A Transfer Network Linking Earth, Moon, and the Triangular Libration Point Regions in the Earth-Moon System. Ph.D. Disser-



(a) $\mathcal{H}_{c,i1}$ ($\Delta t = 159.56$ days)



(b) $\mathcal{H}_{c,i2}$ ($\Delta t = 142.83$ days) (c) L_1 Lyapunov \mathcal{H}_o ($\Delta t = 142.99$ days)

Fig. 14. Maneuver-free connections between the L_1 Lyapunov orbit and the $p = 3$ DRO constructed through interactive selection of manifold intersection states.

tation, School of Aeronautics and Astronautics, Purdue University, West Lafayette, Indiana, 2016.

[2] J. M. Danby. *Fundamentals of Celestial Mechanics*. Willmann-Bell, Inc., Richmond, Virginia, 2nd edition, 1992.

[3] J. Demeyer and P. Gurfil. Transfer to Distant Retrograde Orbits Using Manifold Theory. *Journal of Guidance, Control, and Dynamics*, 30(5), 2007.

[4] J. England, B. Krauskopf, and H. Osinga. Computing One-Dimensional Global Manifolds of Poincaré Maps by Continuation. *SIAM Journal of Applied Dynamical Systems*, 4(4):1008–1041, 2005.

[5] J. S. Eterno. Attitude Determination and Control. In W. J. Larson and J. R. Wertz, editors, *Space Mission Analysis and Design*, pages 354–380. Microcosm Press, El Segundo, California, 1999.

[6] J. Guckenheimer and P. Holmes. *Nonlinear Oscillations, Dynamical Systems, and Bifurcations of Vector Fields*. Springer-Verlag, New York, 1983.

[7] A. Haapala and K. C. Howell. Trajectory Design Strategies Applied to Temporary Comet Capture Including Poincaré Maps and Invariant Manifolds. *Celestial Mechanics and Dynamical Astronomy*, 116(3):299–323, July 2013.

[8] W. S. Koon, M. W. Lo, J. E. Marsden, and S. D. Ross. Heteroclinic Connections between Periodic Orbits and Resonance Transitions in Celestial Mechanics. *Chaos*, 10(2):427–469, 2000.

[9] A. J. Lichtenberg and M. A. Leiberman. *Regular and Chaotic Dynamics*. Springer-Verlag, New York, New York, 2nd edition, 1992.

[10] M. W. Lo, R. L. Anderson, G. Whiffen, and L. Romans. The Role of Invariant Manifolds in Low Thrust Trajectory Design (Part I). In *AAS/AIAA Spaceflight Dynamics Conference*, Maui, Hawaii, February 2004. Paper AAS 04-288.

[11] W. H. Press, S. A. Teukolsky, W. T. Vetterling, and B. P. Flannery. *Numerical Recipes: The Art of Scientific Computing*. Cambridge University Press, New York, 3rd edition, 2007.

[12] S. D. Ross, W. S. Koon, M. W. Lo, and J. E. Marsden. Design of a multi-

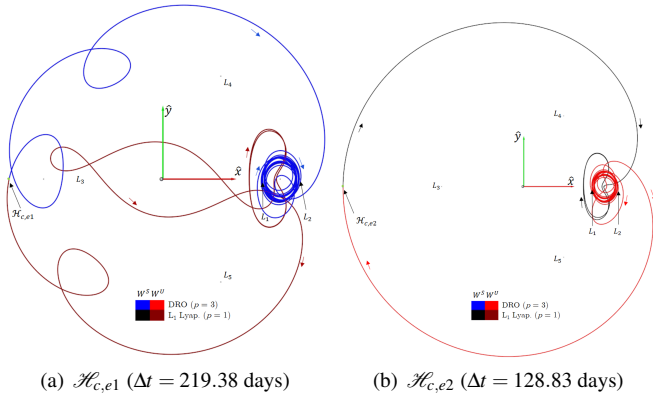


Fig. 15. Maneuver-free connections between the L_1 Lyapunov orbit and the $p = 3$ DRO constructed through interactive selection of manifold intersection states.

moon orbiter. In *AAS/AIAA Space Flight Mechanics Meeting*, Ponce, Puerto Rico, February 2003. Paper AAS03-143.

[13] W. Schlei, K. C. Howell, X. Tricoche, and C. Garth. Enhanced visualization and autonomous extraction of poincaré map topology. *The Journal of the Astronautical Sciences*, pages 1–28, 2015.

[14] S. H. Strogatz. *Nonlinear Dynamics and Chaos*. Westview Press, Perseus Books Publishing, Cambridge, Massachusetts, 1994.

[15] V. Szebehely and H. Mark. *Adventures in Celestial Mechanics*. John Wiley and Sons, Inc., New York, New York, 2nd edition, 1998.

[16] T. M. Vaquero Escribano. Poincaré Sections and Resonant Orbits in the Restricted Three-Body Problem. M.S. Thesis, School of Aeronautics and Astronautics, Purdue University, West Lafayette, Indiana, 2010.

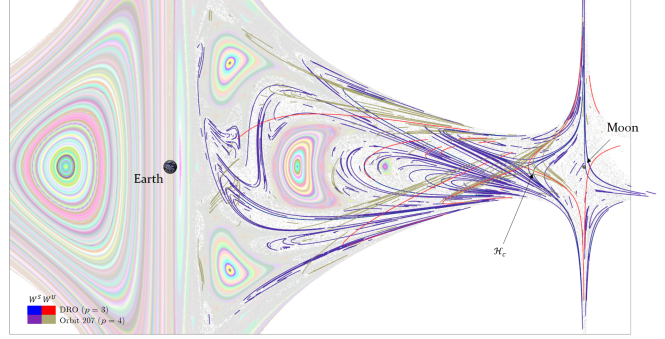
[17] X. Tricoche, C. Garth, and A. Sanderson. Visualization of Topological Structures in Area-Preserving Maps. *IEEE Transactions on Visualization and Computer Graphics*, 17(12):1765–1774, 2011.

[18] M. Vaquero and K. C. Howell. Transfer Design Exploiting Resonant Orbits and Manifolds in the Saturn-Titan System. *Journal of Spacecraft and Rockets*, 50(5):1069–1085, February 2013.

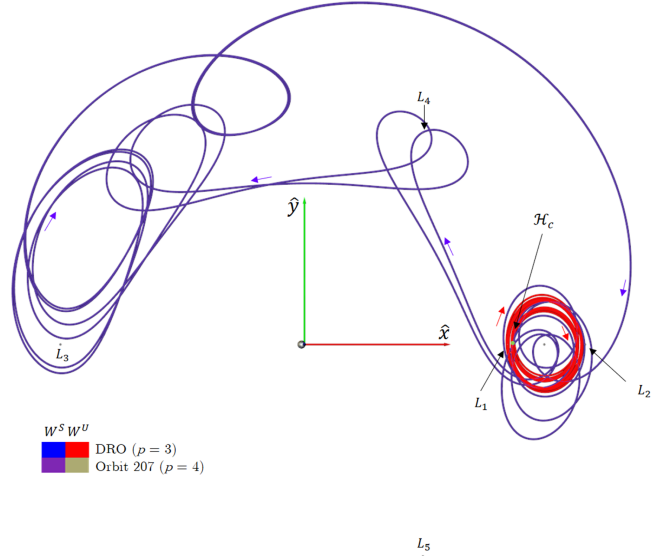
[19] J. R. Wertz. Space Mission Geometry. In W. J. Larson and J. R. Wertz, editors, *Space Mission Analysis and Design*, pages 95–130. Microcosm Press, El Segundo, California, 1999.

[20] J. R. Wertz, R. C. Conger, M. Rufer, N. Sarzi-Amade, and R. E. V. Allen. Methods for Achieving Dramatic Reductions in Space Mission Cost. In *Reinventing Space Conference*, Los Angeles, California, March 2011.

[21] J. R. Yim, J. L. Crassidis, and J. L. Junkins. Autonomous orbit navigation of interplanetary spacecraft. In *AIAA/AAS Astrodynamics Specialist Conference*, Denver, Colorado, August 2000. Paper AIAA 2000-3936.



(a) Manifolds for the $p = 3$ DRO and Orbit O^*



(b) \mathcal{H}_c : $p = 3$ DRO to Orbit O^* ($\Delta t = 197.22$ days)

Fig. 16. Invariant manifolds for the $p = 3$ DRO and Orbit O^* extracted with PMATE and a selected heteroclinic connection in the Earth-Moon system ($C = 2.96$).